Transition metal oxides for kesterite solar cells developed on transparent substrates

Ignacio Becerril-Romero[1], Diouldé Sylla[1], Marcel Placidi[1], Yudania Sánchez[1], Jacob Andrade-Arvizu[1], Victor Izquierdo-Roca[1], Maxim Guc[1], Alejandro Pérez-Rodríguez[1,2], Sigbjørn Grini[3], Lasse Vines[3], Benjamín Pusay[4], Rosa Almache[4], Joaquim Puigdollers[4], Paul Pistor[1,5], Edgardo Saucedo[1,4], and Moisés Espíndola-Rodríguez[1,6]*

[1]IREC - Catalonia Institute for Energy Research, Sant Adrià de Besòs, Spain

[2]Departament d'Enginyeria Electrònica i Biomèdica, IN2UB, Universitat de Barcelona, Barcelona, Spain

[3]University of Oslo, P.O. Box 1048 Blindern, 0316 Oslo, Norway

[4]Universitat Politècnica de Catalunya, Barcelona, Spain

[5]Martin-Luther-University Halle-Wittenberg, Halle (Saale), Germany

[6]DTU – Technical University of Denmark, Lyngby, Denmark

[*]Corresponding author: ibecerril@irec.cat

Abstract

Fabrication on transparent soda-lime glass/FTO substrates opens the way to advanced applications for kesterite solar cells such as semitransparent, bifacial and tandem devices which are key to the future of the PV market. However, the complex behavior of the p-kesterite/n-FTO back interface potentially limits the power conversion efficiency of such devices. Overcoming this issue requires careful interface engineering. This work empirically explores the use of transition metal oxides (TMOs) and Mo-based nanolayers to improve the back interface of CZTSe, CZTS and CZTSSe solar cells fabricated on transparent glass/FTO substrates. Although the use of TMOs alone is found to be highly detrimental for the devices inducing complex current blocking behaviors, the use of Mo:Na nanolayers and their combination with the n-type TMOs TiO_2 and V_2O_5 are shown to be a very promising strategy to improve the limited performance of kesterite devices fabricated on transparent substrates. The optoelectronic, morphological, structural and in-depth compositional characterization performed on the devices suggests that the improvements observed are related to a combination of shunt insulation and recombination reduction. This way, record efficiencies of 6.1%, 6.2% and 7.9% are obtained for CZTSe, CZTS and CZTSSe devices, respectively, giving proof of the potential of TMOs for the development of kesterite solar cells on transparent substrates.

Introduction

The substitution of metallic back contacts by transparent electrodes in photovoltaic (PV) devices fabricated on soda-lime glass (SLG) substrates opens the way to a manifold of advanced applications. This is especially relevant in the case of inorganic thin film technologies with tunable bandgaps like $Cu(In,Ga)Se_2$ (CIGS) and $Cu_2ZnSn(S,Se)_4$ (CZTSSe or kesterite) in which the use

of transparent electrodes combined with wide bandgaps and reduced absorber thicknesses enable the fabrication of highly stable semi-transparent devices[1]. These have a direct application as bifacial solar cells, in building integrated photovoltaics (BIPV) and as top cells in tandem devices. These advanced concepts have the potential to push thin film PV towards higher power densities and lower costs and are likely to play an important role in the future mass deployment of PV. While the CIGS technology has reached efficiencies close to those of Si[2], the scarcity of In and Ga sets a limit to its future module production below the TW/year level[3,4]. In this regard, kesterite-based PV devices present a larger potential since they are composed by Earth-abundant and low-toxicity elements. Thus, the development of this technology on transparent substrates may be of great relevance for the future of inorganic thin film photovoltaics.

Transparent conductive oxides (TCOs) are commonly employed as front electrodes in CIGS and CZTSSe and are also the best choice to replace Mo (the standard back electrode material for these technologies) in order to achieve substrate transparency. Among the different TCOs, the high thermal stability of FTO (compared to other TCOs like AZO and ITO)[5,6] and its Earth-abundant composition make it an ideal candidate for kesterite-based devices. The possibility of directly (i.e. without any additional interfacial layers) employing SLG/FTO substrates for the fabrication of efficient kesterite devices has already been demonstrated with efficiencies of up to 5.7% for CZTSe[5], 4.7% for CZTS[7] and 2.6% for CZTSSe[8]. Although promising, these efficiency values are well below those of the best kesterite devices fabricated on standard opaque SLG/Mo substrates[9–11]. One of the main reasons of this performance difference lies at the non-ohmic and complex behavior of the p-kesterite/n-TCO back interface that may hinder charge extraction[5,12]. However, different interface engineering strategies can be employed in order to reduce or even prevent these issues. A possible approach, is to imitate standard Mo-based devices[13–17] and add a thin Mo(S_xSe_{1-}

$_x)_2$ buffer layer between the TCO and the absorber to enhance the ohmicity of the back interface. We already demonstrated this concept for CZTSe and CZTSSe solar cells fabricated on SLG/FTO and observed a large performance enhancement (around 2.5 fold increase in efficiency) by depositing a 20 nm Mo layer (which was completely selenized during absorber synthesis) on the substrate[8,18]. The performance of such devices was further increased by substituting Mo by Na-doped Mo (Mo:Na), which was attributed to the fact that FTO may act as a barrier for Na diffusion from SLG[8].

Another possible way of enhancing the kesterite/TCO interface is through the use of hole-selective interlayers that may improve charge collection. In this regard, thin layers of transition metal oxides (TMOs) have been employed as hole injectors and extractors for a long time in organic electronics due to their high work function and the possibility of low temperature deposition[19,20]. In addition, they feature a high optical transparency. Thus, on paper, TMOs may possess the right properties to improve the back interface of kesterite solar cells fabricated on SLG/FTO transparent substrates. The idea of using TMOs as hole extractors in inorganic PV has already been successfully tested on CdTe[21], CIGS[22], kesterites[13,23–25] and, more extensively, on c-Si solar cells[26–30]. In the case of kesterites, only the combination of Mo oxides with opaque back contacts has been reported so far. Antunez et al. achieved V_{oc} improvement of 92 mV in a high-efficiency (>11%) CZTSSe device by exfoliating it from its SLG/Mo substrate and depositing a new MoO_3 (20 nm)/Au (100nm) back contact onto it[23]. Similarly, Ranjbar et al. used a 10 nm MoO_3 layer on top of Mo which increased significantly the minority carrier lifetime and V_{oc} of the devices[24]. Liu et al. found similar effects on Cd-doped devices and attributed them to a change in band alignment that was enhancing electron back reflection[25]. Finally, López-Marino et al. used a thin (20 nm) MoO_2 interlayer within a trilayer Mo configuration as a selenization barrier in CZTSe

devices and observed a 67 mV increase of the V_{oc}[13]. Nevertheless, there is a lack of research on exploring the potential of TMOs as hole-selective layers in kesterite PV devices fabricated on transparent substrates.

The work presented here aims at filling this gap by providing an empirical screening on the effect of depositing thin interlayers (5-20 nm) of a wide selection of TMOs (MoO_3, V_2O_5, TiO_2, NiO, Co_3O_4 and CuO) onto transparent SLG/FTO substrates and of combining these oxides with Mo:Na nanolayers to fabricate CZTSe, CZTS and CZTSSe solar cells. The work is divided in four main parts: i) CZTSe solar cells are fabricated onto the different SLG/FTO/TMO and SLG/FTO/TMO/Mo:Na substrate configurations in order to study their suitability for enhancing the FTO/kesterite interface, ii) the best cases are further studied to confirm the most adequate configurations, iii) these are transferred to wide bandgap CZTSSe and CZTS solar cells and iv) morphological, structural and in-depth compositional characterization is performed on the devices. Promising record efficiencies of 6.1%, 6.2% and 7.9% are obtained for CZTSe, CZTS and CZTSSe devices, respectively, giving proof of the potential of TMOs for the development of kesterite solar cells on transparent substrates.

Experimental

Substrate description and sample preparation

The substrate configurations studied in this work were fabricated on commercial FTO-coated SLG. Two different commercial substrates were employed. In the first part of the work (referred to as series A), where an initial screening of the different TMOs is carried out, a 1.6 mm thick SLG/FTO substrate (15 Ω/□, *Kaivo*) was used. For the rest of the work, where only a small selection of TMOs is studied, a 2.2 mm SLG/FTO substrate (7 Ω/□, *Sigma-Aldrich*) was utilized. In both cases, prior to their use, the substrates were submitted to an ultrasonic bath cleaning process

with the following solvent sequence: acetone, isopropanol and deionized water. The time of the ultrasonic treatment in each solvent was approximately 10 minutes at a temperature of 55°C. The substrates were then dried with a nitrogen flux.

The SLG/FTO substrates were coated with different thicknesses (5, 10 and 20 nm) of a wide selection of TMOs by thermal evaporation (*Oerlikon Univex 250*). Substrate configurations without and with Mo:Na were investigated where additionally to the TMOs, also a 20 nm Mo:Na layer was added by DC magnetron sputtering (*Alliance CT100*). Due to the complex nature of the p-kesterite/n-FTO interface, n-type (MoO_3, V_2O_5 and TiO_2) and p-type (NiO, Co_3O_4 and CuO) TMOs were studied. The main optoelectronic properties of these oxides are summarized in **Table 1**. Nevertheless, it should be noted that the properties of the TMOs are known to be strongly related to their oxidation state which is heavily influenced by the deposition conditions and air exposure[27,31]. Finally, it should be borne in mind that evaporated TMOs are rarely stoichiometric and are usually denoted in the literature as MoO_x, V_2O_x, etc.[19]. However, they will be designated with their stoichiometric formulation throughout this work.

The general device fabrication procedure employed throughout the work was similar for all samples. However, further development and work strategy led to slight variations in the final stages of the fabrication process. For the sake of clarity, the different sets of samples have been named as series A, B and C. Below, the general procedure followed for the fabrication of the different samples as well as the particularities of each series are detailed.

General procedure

Cu/Sn/Cu/Zn metallic precursor stacks with Cu/(Zn+Sn)~0.76, Zn/Sn~1.1 composition were deposited by DC magnetron sputtering (*Alliance Ac450*) on the different substrate configurations. The precursors were introduced in a graphite box containing Sn, Se and/or S (*Alfa-Aesar*, powder,

99.999% purity) and submitted to a 2-step thermal reactive annealing in a tubular furnace (*Hobersal*) in order to synthesize the kesterite absorbers. The annealing conditions were different for pure Se, pure S and S/Se solid solution kesterite absorbers and are summarized in **Table 2**. The as-annealed absorbers were then subjected to a chemical etching in $(NH_4)_2S$ in order to remove surface secondary phases[32]. Then, the devices were completed with a CdS buffer layer (chemical bath deposition) as well as an i-ZnO (50 nm)/ITO (200 nm) bilayer (50-80 Ω/□) (DC magnetron sputtering, *Alliance CT100*).

Series A: Screening of TMOs for CZTSe solar cells

The SLG/FTO substrates were coated with 5, 10 and 20 nm layers of MoO_3, V_2O_5, TiO_2, NiO, Co_3O_4, or CuO. Then, either 10 nm of NaF (thermal evaporation, *Oerlikon Univex 250*) or 20 nm of Mo:Na were deposited on top of the different substrate configurations prior to the deposition of the metallic precursor stacks. The precursors were submitted to a reactive annealing under Se+Sn atmosphere. Devices were finished with CdS/i-ZnO/ITO.

Series B: Best performing TMOs on optimized CZTSe device configurations

The SLG/FTO substrates were coated with 5, 10 and 20 nm of V_2O_5 or TiO_2 followed by a 20 nm Mo:Na layer. Prior to the reactive annealing, a 10 nm Ge nanolayer was deposited on top of the metallic precursor stacks (thermal evaporation, *Oerlikon Univex 250*)[33]. The precursors were submitted to a reactive annealing under Se+Sn atmosphere. The completion of the devices with CdS/i-ZnO/ITO was followed by the deposition of an Ag metallic grid and a MgF_2 anti-reflective coating (thermal evaporation, *Oerlikon Univex 250*).

Series C: Technology transfer to wide-bandgap CZTS and CZTSSe and further characterization

The SLG/FTO substrates were coated with 10 nm of V_2O_5 or TiO_2 followed by a 20 nm Mo:Na layer. Prior to the reactive annealing, a 10 nm Ge nanolayer was deposited on top of the metallic

precursor stacks. The precursors were submitted to a reactive annealing under S+Sn or S+Se+Sn atmosphere. The completion of the devices with CdS/i-ZnO/ITO was followed by the deposition of an Ag metallic grid and a MgF_2 anti-reflective coating.

Characterization

The transmittance of the different substrate configurations was investigated before and after being submitted to a selenization process using UV-vis-NIR spectroscopy (*Perkin Elmer Lambda 950*). The analysis was carried out from 300 to 1500 nm. The average transmittance was estimated by integrating the spectra in different spectral regions and calculating the mean value. In order to evaluate the transparency of the substrates, the visible region was defined from 435 to 670 nm following the work by Lunt et al.[34]. In addition, the different TMOs (20 nm) were deposited onto a quartz substrate to avoid the near-UV absorption of SLG and enable the calculation of their bandgap from the inflexion points of their transmittance spectra. In this case, the spectra were acquired from 200 to 1500 nm.

The sheet resistance of the different substrate configurations was measured using a 4-point probe (*Everbeing*).

The J-V characteristics of the devices were obtained under simulated AM1.5 illumination (1000 W/m^2 intensity at room temperature) using a pre-calibrated Class AAA solar simulator (*Abet Technologies Sun 3000*). The external quantum efficiency (EQE) of the devices was measured using a spectral response system (*Bentham PVE300*).

Raman scattering measurements were made under a 785 nm excitation wavelength on complete devices. The measurements were performed both at the front and the back side of the samples. A diameter of 50 μm and an excitation power density below 200 W/cm^2 were used in order to inhibit thermal effects in the spectra while light collection was made through a x20 objective. A 785 nm

excitation wavelength was employed due to its low interaction with the SLG/FTO substrate (for back measurements) and the upper window layer (for front measurements) that allows to characterize the absorber without exfoliating it from the substrate or removing the CdS/ZnO/ITO layers, respectively[35].

Field emission scanning electron microscopy (FESEM) secondary electron imaging (*ZEISS Series Auriga*) was employed to examine the morphology of the full devices in cross-section configuration using an acceleration voltage of 5 kV and working distances of around 5 mm.

The elemental depth profiles of the full kesterite solar cells were measured by secondary ion mass spectroscopy (SIMS) using a magnetic sector *Cameca 7f* microprobe. The analysis was made with a 5 kV Cs^+ primary beam. The elements were measured as MCs^+ cluster ions, where M is the element to be analyzed. Additional measurements were performed in O_2^+ positive mode to confirm the elemental identification, and in particular that of Ti.

Results

Series A: Screening of TMOs for CZTSe solar cells

Before employing the different TMOs within kesterite devices fabricated on SLG/FTO transparent substrates, their transparency and influence on back contact sheet resistance was evaluated before and after a selenization process to assess their compatibility with the CZTSe solar cell fabrication process. The as-deposited TMOs exhibit a great transparency with transmittance levels between 71% and 93% in the visible range and even higher in the IR as shown in **Figure S1**, **Figure S2, Table S1** and **Table S2**. This result is surprising since the reported bandgaps of some of the oxides studied here are quite narrow and, therefore, higher above-bandgap absorption was expected. In order to shed light onto this matter, the bandgaps of the different TMOs were

calculated from transmittance spectra (see **Figure S2**) and are shown in **Figure 1**. It can be observed that the values obtained are much higher than those reported in the literature (see **Table 1**) which matches our observations. The origin of such wide bandgaps will be discussed later on. On the other hand, the sheet resistance of the as-deposited TMO-containing back contacts does not vary noticeably with respect to the SLG/FTO reference (R_{sheet} ~15 Ω/□). This value is significantly improved (~9 Ω/□) after submitting the different substrate configurations to a selenization annealing process. However, the selenization process is also observed to affect negatively the optical transmittance of some of the oxides in the visible and, specially, in the IR regions (see **Figure S1** and **Table S1**). NiO, Co_3O_4, and MoO_3 exhibit the most degraded transmittances which can be attributed to the formation of narrow-bandgap selenide compounds like Ni_3Se_2 (E_g~1.4 eV[36]), CoSe (E_g~1.5 eV[37]) and $MoSe_2$ (E_g~1.1 eV[38]). Oppositely, V_2O_5, CuO and TiO_2 show improvement or almost no degradation after annealing.

In order to empirically evaluate the suitability of the different TMOs for their use at the back contact, CZTSe solar cells were fabricated on every SLG/FTO/TMO substrate configuration. A 10 nm NaF layer was deposited onto the substrates prior to the deposition of the Cu-Zn-Sn metallic precursor to compensate the possible Na-blocking behavior of FTO[8] and/or the TMOs. The J-V curves and optoelectronic parameters of the best devices found in each substrate configuration are shown in **Figure 2** (as dashed lines) and **Table S3**, respectively. The device fabricated directly on the SLG/FTO reference substrate (dashed line in **Figure 2 a**) exhibits a low V_{oc} (255 mV) that limits its efficiency to 2.9%. The shape of the curve suggests that the main issue of the device may be a low shunt resistance (R_{sh}) which would explain the low V_{oc} observed. The addition of 5 to 20 nm layers of the different TMOs (dashed lines in **Figure 2 b-g**) proves to be very detrimental for the devices introducing complex thickness-dependent current blocking behaviors that completely

distort the shape of the J-V curves and result in device efficiencies well below the SLG/FTO reference. However, this is not the case for a 20 nm MoO_3 layer for which no current blockage is detected and the V_{oc} is highly enhanced (344 mV) leading to a significantly higher efficiency (3.8%) than in the SLG/FTO reference substrate. Based on the transmittance measurements of the SLG/FTO/MoO_3 substrate configuration (dashed line in **Figure S1 a**) this beneficial effect can be attributed to the formation of a $MoSe_2$ interlayer between the kesterite absorber and the FTO, rather than to the use of the oxide itself. In order to confirm this result, CZTSe solar cells were fabricated on SLG/FTO coated with either 20 nm of Mo (with no additional NaF layer) or Mo:Na. The results are shown in the first two rows of **Table S4** and in **Figure 2 a** (solid lines). It can be observed that Mo:Na leads to significantly higher V_{oc} and FF than the bare Mo (which is consistent with our previous results and attributable to a higher Na incorporation into the absorber[8]). Moreover, the observed V_{oc} improvement is analogous to that obtained when employing MoO_3 (with NaF, **Figure 2 b**) thus confirming that the beneficial effects observed with this oxide are probably related to the formation of $MoSe_2$.

In view of these results, the different TMOs were tested again but combined with a 20 nm Mo:Na layer deposited on top of them. The results are shown in **Table S4** and as solid lines in **Figure 2 b-g**. Unexpectedly, the combination of Mo:Na and MoO_3 results in highly degraded devices. However, substantial improvements are observed for the other TMOs when they are combined with Mo:Na. Some similarities can be detected between the TMOs that were observed to get selenized during the annealing process (NiO and Co_3O_4) and the TMOs which seemed mostly unaffected by it (V_2O_5, CuO and TiO_2). Regarding the first group, the addition of Mo:Na tends to reduce current blocking and to improve the V_{oc} of the devices with respect to the bare TMOs. Despite these improvements, none of the devices surpasses the performance of the

SLG/FTO/Mo:Na reference due to a low J_{sc}, which may indicate that some current blocking still remains in the devices. As for the Se-inert TMOs, all of them exhibit radical improvements with the addition of Mo:Na. The distortion observed in the J-V curves for the bare TMOs completely disappears with improved V_{oc}, J_{sc} and FF. In the case of TiO_2 and V_2O_5 combined with Mo:Na, efficiencies much higher than the SLG/FTO/Mo:Na reference are obtained. For TiO_2, similar improvements are achieved with 5 and 10 nm TMO layers with enhanced V_{oc} and FF resulting in a maximum efficiency of 4.9% for a 10 nm layer. A thicker TiO_2 layer seems to further enhance V_{oc}, but also to induce a higher series resistance with lower FF and J_{sc} that hinders the overall performance of the device. As for V_2O_5, a very similar V_{oc} enhancement is observed regardless of the thickness of the layer. However, the J_{sc} and FF of the devices increases with the increasing TMO layer thickness leading to a 4.8% efficiency for a 20 nm layer.

Series B: Best performing TMOs on optimized CZTSe device configurations

The reference samples with and without Mo:Na as well as the best performing substrate configurations (SLG/FTO/TiO_2/Mo:Na and SLG/FTO/V_2O_5/Mo:Na) were further studied to check the reproducibility of the previous results in our optimized device structure that includes a 10 nm Ge layer[33], a metallic grid and an anti-reflecting coating (see experimental section). The same TMO thickness screening (5, 10 and 20 nm) as in series A was performed. **Table 3** shows the main optoelectronic parameters of the record device of each sample together with their calculated series and shunt resistances. Complementarily, **Figure S3** shows more global trends of the samples through a boxchart of the main solar cell parameters. Compared to series A, the SLG/FTO reference performs better (3.8% maximum efficiency) as a result of the improved device configuration. Nevertheless, it is confirmed that the V_{oc} is still the main limiting factor of the device. The presence of strong shunt paths speculated before is numerically proved: on the one

hand, the device exhibits a very low R_{sh} value (60 $\Omega \cdot cm^2$) and, on the other hand, it also presents the lowest R_s, by far, among all the substrate configurations. These two observations combined indicate that there exist channels or paths within the device through which the carriers can travel with low resistance. However, other possible problems like an insufficient grain boundary passivation cannot be discarded. Similarly to series A, a 20 nm Mo:Na layer on top of the SLG/FTO substrate significantly enhances the V_{oc} and FF of the devices resulting in a 5.0% maximum efficiency. These improvements are mainly related to a reduction of shunting since both R_{sh} and R_s are highly increased (by a factor of 4 and 2, respectively). The combination of TiO_2 and V_2O_5 with Mo:Na leads to further improvements confirming the profound impact of these oxide nanolayers. In the case of TiO_2, a large improvement of all solar cell parameters is observed regardless of the thickness employed. However, **Figure S3** indicates that a 20 nm layer leads to a lower average J_{sc} and to higher dispersion suggesting series resistance issues in agreement with series A (this is not reflected in **Table 3** since the record device corresponds to an extreme outlier not representative of the global tendency of the sample). The best device is obtained with a 10 nm TiO_2 layer. Compared to the SLG/FTO/Mo:Na reference, there is an average improvement of 65 mV in V_{oc}, 5% (absolute) in FF and 2.2 mA/cm^2 in J_{sc}. All this leads to a remarkable 6.2% record efficiency. **Table 3** indicates that these enhancements can be attributed to a highly increased shunt resistance (twice higher than that of the Mo:Na reference). In the case of V_2O_5, improvements with respect to the SLG/FTO/Mo:Na reference are only achieved with a 10 nm layer which moderately enhances the average V_{oc} and FF resulting in a 5.4% maximum efficiency. However, the origin of these improvements is not clear from the data presented here.

To further explore the effects of the different substrate configurations, the EQE of the record devices was also measured (**Figure 3**). The SLG/FTO reference presents an almost linearly

decreasing collection of photogenerated charges from 500 nm (80%) to 1200 nm (40%). The addition of Mo:Na enhances collection in that range with the highest improvement observed around 950 nm. However, the shape of the EQE remains rather linear. The substrate configurations containing TMOs present complex and thickness-sensitive behaviors. In the case of V_2O_5 (**Figure 3**, bottom), the only significant improvement is found for a 10 nm layer, which slightly boosts collection in the 500-1200 nm range compared to the SLG/FTO/Mo:Na reference. As for TiO_2 (**Figure 3**, top), charge collection is substantially increased with respect to the other substrate configurations in the 800-1200 nm spectral range when employing either a 5 or a 10 nm layer. Increasing the thickness of the TiO_2 layer to 20 nm maintains an improved collection for wavelengths larger than 900 nm but causes it to significantly drop in the 500-900 nm range changing the shape of the EQE curve and suggesting a possible influence of TiO_2 not only at the back but also towards the front interface.

Series C: Technology transfer to wide-bandgap CZTS and CZTSSe and further characterization

Once the benefits of employing TMO-containing substrate configurations were proven for narrow-bandgap CZTSe-based devices, this concept was transferred to wide-bandgap kesterites. CZTS and CZTSSe (S/S+Se~0.9) devices were fabricated on the reference substrates and on the best TMO configurations: 10 nm of TiO_2 and V_2O_5. **Table 4** shows the main optoelectronic parameters of the record devices together with their calculated series and shunt resistances. From these data, it is clear that similar shunting problems to those observed in CZTSe are detected for CZTS and CZTSSe devices fabricated directly on the reference SLG/FTO substrate. However, series resistance is also a very limiting issue in these wide bandgap kesterite absorbers which results in solar cells with efficiencies slightly below those of CZTSe. As in the case of CZTSe, the addition of Mo:Na and subsequent formation of $Mo(S_x,Se_{1-x})_2$ is observed to reduce shunting both

for CZTS and CZTSSe devices. In addition, the series resistance of the devices is also highly diminished. Despite these general trends, very dissimilar behaviors are observed for CZTS and CZTSSe when Mo:Na and TMOs are added to the SLG/FTO substrates. In the case of CZTS, it can be observed that the shunting reduction effect of Mo:Na is very strong (5-fold increase of shunt resistance) compared to CZTSe and CZTSSe which, among other factors, leads to a 755 mV V_{oc} (176 mV increase) and a 6.1% efficiency, the highest reported for a pure sulfide kesterite fabricated on a transparent substrate. Regarding the use of TMOs, the addition of V_2O_5 eliminates most of the shunting insulation provided by Mo:Na while TiO_2 induces a very high R_s degrading the performance of the devices in both cases. As for CZTSSe, although Mo:Na greatly reduces the R_s of the device, this value is still around twice higher than for CZTSe and CZTS samples with a similar substrate configuration which limits the maximum efficiency to 5.2%. On the other hand, the combination of Mo:Na with 10 nm of V_2O_5 and TiO_2 causes strong improvements on the devices, especially on their R_{sh}. In the case of TiO_2, a 6.4% efficiency is achieved thanks to a highly improved FF. However, a high R_s is still present in the device. In the case of V_2O_5, similar FF improvements are observed together with a significantly reduced R_s, which results in a device with a 3.6 mA/cm^2 higher J_{sc} compared to the SLG/FTO/Mo:Na reference substrate. This ultimately leads to a 7.9% record efficiency device. To the best of our knowledge, this is the highest efficiency reported for a kesterite-based device fabricated on a transparent substrate.

Morphological, structural and in-depth compositional characterization

The influence of the different substrate configurations on the morphology of the different kesterite absorbers was studied by FESEM. **Figure 4** shows cross-sectional micrographs of the CZTSe, CZTS and CZTSSe devices fabricated on the different substrate configurations. In the case of CZTSe, no significant differences can be spotted in the morphology of the absorbers despite

the different back interfaces employed. All of them present large micron-sized grains and a compact structure. Oppositely, the substrate configuration is found to completely change the morphology of CZTS absorbers. The device fabricated directly on SLG/FTO presents a small crystallite porous structure with numerous voids at the bottom. The addition of Mo:Na increases grain size and results in a more compact morphology. However, the combination of TiO_2 and V_2O_5 with Mo:Na largely hinders crystal growth resulting in a morphology dominated by small crystallites with a similar appearance to the SLG/FTO reference substrate. As for CZTSSe, the absorber synthesized on SLG/FTO exhibits large grains although combined with abundant voids and crystallites at the bottom. The addition of Mo:Na does not modify the morphology substantially. However, the inclusion of a 10 nm TiO_2 or V_2O_5 layer largely increases crystal size and compactness completely eliminating any sign of crystallites and voids and yielding large columnar grains with a reduced number of grain boundaries.

The CZTSe, CZTS and CZTSSe devices fabricated on the different substrate configurations were measured with Raman spectroscopy from their front and back sides. The resulting spectra are shown in **Figure 5.** In general, no significant differences can be observed in the position and full width at half maximum (FWHM) of the main kesterite peaks regardless of the absorber, substrate configuration employed or the side of the sample measured. In addition, there is no trace of secondary phases in CZTSe and CZTSSe devices neither at the front nor at the back of the absorbers. This is particularly revealing in the case of CZTSe since the excitation wavelength employed is resonant with the bandgap of $SnSe_2$[39,40] whose formation could be a priori expected when working with an FTO back contact. In the case of CZTS, some SnS is detected at the front surface of the devices fabricated on SLG/FTO and SLG/FTO/Mo:Na. On the other hand, the back measurements of the CZTSe devices confirm the formation of $MoSe_2$ when Mo:Na is employed

at the back. It should be noted that MoS_2 and $Mo(S,Se)_2$ are not detected in CZTS and CZTSSe devices since their wider bandgap and reduced thickness make them transparent to the excitation laser source employed (785 nm). Additionally, the S/(S+Se) compositional ratio of the CZTSSe devices was analyzed to reveal if the different substrate configurations could affect the anionic composition of the absorbers. This was done employing a peak area ratio method similar to the one developed by Dimitrievska et al.[41] and recently adapted to the 785 nm excitation wavelength[42]. No significant compositional differences are observed with the S/(S+Se) ratios ranging from 0.86 to 0.91.

In order to shed light on the role and location of the different layers added to the FTO back contact as well as on Na diffusion and incorporation, the best performing CZTSe, CZTS and CZTSSe devices were analyzed by SIMS (**Figure 6**). Na is observed to accumulate at the back kesterite/FTO interface in every case which is expectable since the Mo:Na layer was deposited there and Na has been demonstrated to assist the formation of $MoSe_2$ and incorporate into it[43,44]. In addition, there is also an accumulation of Na towards the kesterite/CdS interface. This indicates that Na is effectively diffusing from the back to the front of the absorbers when employing Mo:Na nanolayers. The accumulation of Na at the front interface is more pronounced in the case of CZTS which suggests that the smaller grain size (or larger amount of grain boundaries) of the absorber observed by FESEM (**Figure 4**) promotes the diffusion of this alkali metal. However, it is not straightforward to quantitatively compare Na incorporation onto the different absorbers due to possible matrix effects between sulfide and selenide kesterites which may change the ionization energy of Na and, therefore, the intensity of the SIMS signal. Regarding the TMOs, clear signals of V (spectrum d) and Ti (only in O_2^+ mode, spectrum b) are found at the back interface of CZTSSe and CZTSe absorbers. This gives proof of their stability and their presence at the back after the

kesterite synthesis process and confirms that the effects observed in the optoelectronic properties of the devices can be truly ascribed to the presence of these TMOs at the back interface. Interestingly, in the case of Ti, an accumulation at the front interface is also observed which could point towards a diffusion of this metal through the absorber. It was shown before that 20 nm of TiO_2 modify the EQE response in the 500-900 nm range (see **Figure 3**) which may be related to the observed Ti accumulation towards the CdS/kesterite interface. However, this Ti signal could also be arising from mass interference with other elements.

Discussion

TMO bandgap

It has been shown that the measured bandgaps of the different TMOs are much higher, in general, than those usually reported in the literature (see **Figure 1** and **Table 1**). This can be attributed to the small crystallite size and/or the amorphous nature of the nanometric layers deposited in this work (expectable since the deposition was carried out at room temperature). It has been extensively reported that the bandgap of nanometric semiconductor crystallites follows a logarithmic trend with the increasing grain size due to quantum confinement effects[45–48]. In order to confirm this possible cause for the high bandgaps observed, the bandgap of MoO_3 was investigated for different layer thicknesses (20, 40 and 80 nm) (inset of **Figure 1**). In effect, the bandgap is found to decrease approximately logarithmically with the increasing layer thickness and to approach the bulk values reported in the literature for an 80 nm layer. On the other hand, it should also be taken into account that the evaporated oxides are likely to be very defective. This may generate very low correlation distances (even below crystallite size) of their crystal structure which can further increase quantum confinement effects[49]. In addition, the modification of the band structure that follows quantum

confinement may vary the allowed transitions compared to bulk materials and shift the bandgap from a narrow indirect to wide direct one. The extremely large bandgap shifts observed for CuO and Co_3O_4 with respect to the values reported in **Table 1** (+2.6 eV for CuO and +3 eV for Co_3O_4) together with the Tauc plots shown in Figure S4 fit with this explanation. In the case of CuO, this is further supported by experimental observations made in the field of nanoparticle synthesis. Lim et al. observed the coexistence of both an indirect (1.4 eV) and a direct (3.1 eV) bandgap when analysing the optical properties of 80 nm CuO nanoparticles[50]. In addition, Arun et al. reported a direct 4.2 eV bandgap for 20 nm CuO nanoparticles[51]. These results fit with the bandgap observed in this work for CuO and give further prove of the small crystallite size of the evaporated layers. On the other hand, no information about such a wide direct bandgap for Co_3O_4 nanoparticles has been found in the literature. However, He et al. reported a 4.0 eV bandgap for 33 nm CoO nanoparticles[52]. Thus, it may be possible that, apart from quantum confinement, the oxidation state of Co_3O_4 powder changed during evaporation which could explain the high bandgap observed for this TMO. Finally, V_2O_5 has shown two clear inflexion points corresponding to a 2.75 eV (similar to bulk values) and a 4.13 eV bandgap. However, it is not clear from the data presented in this work that the large difference between both values can be ascribed solely to quantum confinement effects or to changes in the oxidation state and further investigation is required.

Limitations of the kesterite/FTO interface

The results obtained in this work show that series resistance is not a critical issue when fabricating CZTSe solar cells on SLG/FTO substrates. This contradicts previous works in which R_s was reported to be a limiting factor for the performance of CZTSe solar cells fabricated on FTO[5,8,18]. However, a near-ohmic behavior with no R_s issues could be expected a priori regarding the work functions reported in the literature for CZTSe and FTO which show a favorable band

alignment as depicted in **Figure 7 a** (although this should be taken with great care since the properties of CZTSe and FTO can vary considerably depending on their fabrication process). On the contrary, the series resistance has been found to be a critical factor for CZTS and CZTSSe-based devices fabricated directly on FTO. This may be due to the higher work function of S-rich kesterite absorbers leading to a less favorable band alignment as shown in **Figure 7 b**. Nevertheless, in previous works we detected a high reactivity of FTO to annealing processes in S+Se atmosphere leading to a degradation of its conductivity[8]. Thus, the series resistance issues observed could be simply due to an increased resistance of the FTO layer during annealing in pure S and, especially, in S+Se mixture.

On the other hand, the main issue found when fabricating devices directly on SLG/FTO has been found to be a very low shunt resistance regardless of the kesterite absorber. The origin of such a strong shunting is not easy to discern, though. FESEM micrographs (**Figure 4**) show devices with a compact structure and with no evidence of front-back interconnection. It has been reported that some secondary phases like $SnSe_2$ act as shunt paths[40,53]. However, the excitation wavelength employed for the Raman analysis is very sensitive to this compound and no traces of it were found in the SLG/FTO/CZTSe device which presented clear shunting problems. Another possible source of shunting that has not been explored in this work is the presence of conductive grain boundaries. In this respect, Guo et al. reported a low shunt resistance in CZTSe devices and attributed it to Se-poor and Sn-rich grain boundaries exhibiting a metallic behavior and acting as conductive channels[54]. Since, in this work, kesterite devices are fabricated on FTO, a Sn-enrichment of the grain boundaries as an effect of Sn-diffusion from the substrate seems plausible and could lie at the origin of the observed shunting.

In addition to shunting, EQE measurements (**Figure 3**) have also revealed strong collection issues on the CZTSe devices fabricated on SLG/FTO. The low carrier collection observed can be considered to be independent from shunting since, except in extreme cases, shunts can be neglected in short-circuit conditions so they should affect neither the J_{sc} nor the EQE of the devices noticeably. Although **Figure 7** shows an expected favorable band alignment and the CZTSe/FTO and no R_s problems were observed, these EQE results suggest that the CZTSe-FTO coupling is far from ideal which could be originating an extended region with a high density of defects at the back interface leading to strong interface recombination. Furthermore, $MoSe_2$ significantly improves collection. The fact that this layer is located at the back interface and that higher collection improvements are observed for deeply generated charges supports the idea of the back interface acting as a source of recombination. The existence of interface defects is strengthened by the ~10% difference between the J_{sc} value obtained from J-V analysis (31.5 mA/cm^2) and from integrating the EQE curve (28.4 mA/cm^2) which indicates the presence of charged defects that affect collection during low light intensity EQE measurements but are partially neutralized by photogenerated carriers under more intense illumination in J-V curve acquisition.

Role of $Mo(S_x,Se_{1-x})_2$

The formation of $Mo(S_x,Se_{1-x})_2$ on top of the FTO has been observed to alleviate shunting largely increasing the V_{oc} of the devices. This effect could be attributed to $Mo(S_x,Se_{1-x})_2$ acting as an insulating layer between the kesterite and FTO layers and, thus, reducing shunt currents. Besides improving shunting, $Mo(S_x,Se_{1-x})_2$ has also been shown to decrease the large series resistance of CZTS and CZTSSe devices. Regarding the FTO degradation during annealing mentioned above, it is possible that $Mo(S_x,Se_{1-x})_2$ acts as a protective layer and prevents the reaction of S and S-Se species with the FTO thus preserving a good conductivity of the back contact. Contradictorily, the

SLG/FTO/MoO_3/Mo:Na configuration has resulted in a highly degraded device with a large series resistance. López-Marino et al. reported a change in the orientation of the c-axis of $MoSe_2$ when selenizing a 20-30 nm Mo sacrificial layer deposited on SLG/Mo and SLG/Mo/MoO_2 substrates shifting from purely parallel to the substrate (i.e. electrically benign columnar grains) in the former case to a mixture of parallel and perpendicular (i.e. stacked horizontal $MoSe_2$ layers potentially detrimental for R_s) when MoO_2 was present[13]. Thus, it may be possible that the degradation of the R_s observed when combining MoO_3 and Mo:Na is related to the presence of a too thick $MoSe_2$ layer with an electrically unfavorable orientation induced by the presence of the oxide.

On the other hand, EQE measurements have shown that the formation of $MoSe_2$ on top of the FTO improves charge collection in CZTSe devices (see **Figure 3**) which may also be contributing to the V_{oc} improvement associated to this layer. The mechanism through which $MoSe_2$ improves collection is not clear but may be related to an electronically improved interface leading to reduced interface recombination. If highly doped, $MoSe_2$ could be acting as a p^+ accumulation layer reducing the width of the barrier formed at the CZTSe/FTO interface and preventing the formation of an extended defect region. This could also be contributing to the reduction of the series resistance in CZTS and CZTSSe observed with $Mo(S_x,Se_{1-x})_2$. However, the improved collection in CZTSe devices may also be due to the passivation of interface defects. It was observed in **Figure 6** that a large amount of Na remains at the back within the $MoSe_2$ layer. Na is known to passivate defects at the grain boundaries and interfaces in kesterite devices[55–58] Thus, this back Na reservoir may be assisting in passivating such interface defects.

Combination of TMOs and Mo:Na

The addition of TMO layers on top of the FTO for the fabrication of CZTSe devices has been observed to induce a current-blocking behavior and, thus, to be very detrimental for the devices.

However, the combination of the TMOs with Mo:Na ($MoSe_2$), has been found to improve the performance of the CZTSe devices with respect to the case of the bare oxides twofold: i) by reducing or even eliminating the current blocking behavior observed for the bare TMOs and ii) by increasing the V_{oc} of every SLG/FTO/TMO configuration. Although related, both effects seem to have different origins. On the one hand, the V_{oc} increase occurs in, more or less, a similar way in every substrate configuration regardless of the TMO and may be linked, as explained above, to $MoSe_2$ shunt insulation. On the other hand, the reduction of the current blocking behavior can be related to an improved back interface and is particularly stronger for the n-type TMOs: V_2O_5 and TiO_2. The superior performance of combining Mo:Na with n-type TMOs could be tentatively ascribed to a p-CZTSe/p^+-$MoSe_2$/n-TMO/n^+-FTO complex back interface that may be offering a more favorable band coupling. However, the results obtained in Series B also suggest that the presence of these oxides at the back is adding an extra shunt protection to that provided by $MoSe_2$ (see **Table 3** and **Table 4**). Nevertheless, both shunting insulation and a more favorable band coupling can occur simultaneously and the performance enhancements caused by these TMOs are probably a combination of both effects.

In addition, TiO_2 and V_2O_5 have also been observed to assist $MoSe_2$ in reducing recombination (see **Figure 3**). These oxides have been reported to exhibit passivating properties in c-Si so it may be possible that they are also helping in passivating CZTSe/FTO interface defects[28]. However, their passivation effectiveness shows a complex thickness-dependent behavior with a tendency to decrease with the increasing layer thicknesses. Interestingly, by comparing the J-V (**Table 3**) and EQE (**Figure 3**) measurements of the substrate configurations, a non-dependence between shunt insulation and recombination reduction can be spotted. In the case of TiO_2, the EQE profiles for both 5 and 10 nm TMO layers are identical indicating a similar recombination reduction. However,

a much higher shunt resistance is obtained for the 10 nm layer. Likewise, in the case of V_2O_5, shunt resistance increases with the increasing layer thickness while only an enhanced carrier collection is observed for a 10 nm layer. Thus, it is clear that an increased R_{sh} does not necessarily mean reduced recombination and vice versa. This supports the idea that both shunting insulation, a more favorable band coupling and passivation are contributing to improve the devices but also indicates that these processes are rather independent from each other.

The different substrate configurations studied display a similar behavior in CZTSSe and CZTSe devices with the combination of Mo:Na with TiO_2 and V_2O_5 yielding further R_{sh} improvements with respect to the Mo:Na reference. As explained above for the case of CZTSe, both a p-CZTSSe/p^+-Mo(S_xSe_{1-x})$_2$/n-TMO/n^+-FTO favorable back interface and an extra shunt insulation are likely to be the main effects provided by the combination of Mo:Na and n-TMOs. However, comparing the results obtained with CZTSe and CZTSSe devices, it seems that the predominance of one effect or the other depends on the TMO employed. This way, TiO_2 exhibits a higher insulating capacity leading to larger shunt resistances both in CZTSe and CZTSSe. However, this is a double edged sword and TiO_2 also leads to a higher series resistance. On the other hand, V_2O_5 also leads to large performance enhancements with lower R_{sh} than TiO_2 but, at the same time, it does not affect the R_s of the devices noticeably. This suggests that the beneficial effects of TiO_2 might be predominantly related to a low conductivity that aids in shunt insulation while the improvements observed with of V_2O_5 might be principally arising from an electronically improved back interface.

Contrarily to the case of CZTSe, the use of TMOs largely influences the morphology of CZTS and CZTSSe absorbers. In the case of CZTS, the deposition of V_2O_5 and TiO_2 layers leads to a kesterite absorber full of small crystallites which is probably one of the origins of the low

efficiency of the devices. On the contrary, an absorber layer with very large grains is found for CZTSSe when these TMOs are present. A possible explanation of these differences may be that, similarly to the FTO, these oxides are not inert to S during annealing and the resulting layers influence the growth of the layers growing above them.

In order to have a better understanding of the devices and confirm some of the theories expounded above, it would be very useful to perform a band alignment analysis of the different substrate configurations similar to that shown in **Figure 7¡Error! No se encuentra el origen de la referencia.**. However, this task requires detailed information about the electronic properties of the TMOs whose acquisition presents several challenges. First of all, the work function and conductivity of the oxides are known to be strongly related to their oxidation state which is heavily influenced by the deposition conditions during thermal evaporation and air exposure[27,31]. In addition, the TMOs evaporated in this work show bandgap values much larger than those usually reported in the literature due to quantum confinement effects which, logically, strongly modifies their band structure and alignment. Finally, contrarily to the works that study TMOs in c-Si and organic electronics, the TMOs are submitted to a high temperature reactive annealing process which further modifies their properties and induces elemental diffusion in all directions. Thus, all these issues complicate the correct analysis of the band alignment for the kesterite/Mo:Na/TMO/FTO interfaces.

Conclusions

This work demonstrates the viability of fabricating highly efficient kesterite-based devices on transparent SLG/FTO substrates through the combination of thin Mo:Na and TMO nanolayers. This opens the door to advanced kesterite applications such as semitransparent, bifacial and tandem solar cells which are key for the future of the PV market. The main problem observed in

kesterite devices fabricated on SLG/FTO is shunting which can be greatly alleviated using selenized Mo:Na nanolayers on top of the FTO. On the other hand, TMOs have been found to be highly detrimental for the devices inducing complex current blocking behaviors. However, the combination of Mo:Na and 10 nm layers of the n-type TMOs TiO_2 and V_2O_5 have enabled obtaining high efficiency devices. The improvements observed seem to be related to a combination of shunt insulation and recombination reduction. Although this work is mostly an empirical screening and the characterization performed in this work is sufficient only to have a general idea about underlying mechanisms, it renders clear that the use of TMO and/or Mo:Na nanolayers is a very promising strategy to improve the hitherto limited performance of kesterite devices fabricated on transparent substrates. The efficiencies achieved in this work for CZTS (6.1%) and CZTSSe (7.9%) devices are the highest reported for these absorbers using a transparent substrate. As summary and to illustrate the improvements offered by the approach explored in this work, **Figure 8** compares the J-V curves of the reference samples fabricated directly on SLG/FTO and of the record substrate configurations for the different absorbers.

Acknowledgments

This research was supported by the H2020 Programme under the project INFINITE-CELL (H2020-MSCA-RISE-2017-777968), by the Ministry of Science and Innovation of Spain under IGNITE project (ENE2017-87671-C3-1-R), by the European Regional Development Funds (ERDF, FEDER Programa Competitivitat de Catalunya 2007–2013) and CERCA Programme / Generalitat de Catalunya. Authors from IREC belong to the SEMS (Solar Energy Materials and Systems) Consolidated Research Group of the "Generalitat de Catalunya" (Ref. 2017 SGR 862).

References

(1) Sun, J.; Jasieniak, J. J. Semi-Transparent Solar Cells. *Journal of Physics D: Applied Physics* **2017**, *50* (9), 093001. https://doi.org/10.1088/1361-6463/aa53d7.

(2) Solar Frontier Press Release. Solar Frontier Achieves World Record Thin-Film Solar Cell Efficiency of 23.35%. January 17, 2019.
(3) Candelise, C.; Winskel, M.; Gross, R. Implications for CdTe and CIGS Technologies Production Costs of Indium and Tellurium Scarcity: Effects of Indium and Tellurium Scarcity. *Progress in Photovoltaics: Research and Applications* **2012**, *20* (6), 816–831. https://doi.org/10.1002/pip.2216.
(4) Phipps, G.; Mikolajczak, C.; Guckes, T. Indium and Gallium: Long-Term Supply. *Renewable energy focus* **2008**, *9* (4), 56–59.
(5) Kim, J.-S.; Kang, J.-K.; Hwang, D.-K. High Efficiency Bifacial $Cu_2ZnSnSe_4$ Thin-Film Solar Cells on Transparent Conducting Oxide Glass Substrates. *APL Materials* **2016**, *4* (9), 096101. https://doi.org/10.1063/1.4962145.
(6) Nakada, T.; Hirabayashi, Y.; Tokado, T.; Ohmori, D.; Mise, T. Novel Device Structure for Cu(In,Ga)Se_2 Thin Film Solar Cells Using Transparent Conducting Oxide Back and Front Contacts. *Solar Energy* **2004**, *77* (6), 739–747. https://doi.org/10.1016/j.solener.2004.08.010.
(7) Wang, Z.; Tao, J.; Xiao, W.; Xu, T.; Zhang, X.; Hu, D.; Ma, Z. Influence of Deposition Potential on Cu_2ZnSnS_4 Thin–Film Solar Cells Co–Electrodeposited on Fluorine–Doped Tin Oxide Substrates. *Journal of Alloys and Compounds* **2017**, *701*, 465–473. https://doi.org/10.1016/j.jallcom.2017.01.114.
(8) Espindola-Rodriguez, M.; Sylla, D.; Sánchez, Y.; Oliva, F.; Grini, S.; Neuschitzer, M.; Vines, L.; Izquierdo-Roca, V.; Saucedo, E.; Placidi, M. Bifacial Kesterite Solar Cells on FTO Substrates. *ACS Sustainable Chemistry & Engineering* **2017**, *5* (12), 11516–11524. https://doi.org/10.1021/acssuschemeng.7b02797.
(9) Wang, W.; Winkler, M. T.; Gunawan, O.; Gokmen, T.; Todorov, T. K.; Zhu, Y.; Mitzi, D. B. Device Characteristics of CZTSSe Thin-Film Solar Cells with 12.6% Efficiency. *Advanced Energy Materials* **2014**, *4* (7). https://doi.org/10.1002/aenm.201301465.
(10) Taskesen, T.; Neerken, J.; Schoneberg, J.; Pareek, D.; Steininger, V.; Parisi, J.; Gütay, L. Device Characteristics of an 11.4% CZTSe Solar Cell Fabricated from Sputtered Precursors. *Advanced Energy Materials* **2018**, 1703295. https://doi.org/10.1002/aenm.201703295.
(11) Yan, C.; Huang, J.; Sun, K.; Johnston, S.; Zhang, Y.; Sun, H.; Pu, A.; He, M.; Liu, F.; Eder, K.; Yang, L.; Cairney, J. M.; Ekins-Daukes, N. J.; Hameiri, Z.; Stride, J. A.; Chen, S.; Green, M. A.; Hao, X. Cu_2ZnSnS_4 Solar Cells with over 10% Power Conversion Efficiency Enabled by Heterojunction Heat Treatment. *Nature Energy* **2018**, *3* (9), 764–772. https://doi.org/10.1038/s41560-018-0206-0.
(12) Ge, J.; Chu, J.; Jiang, J.; Yan, Y.; Yang, P. Characteristics of In-Substituted CZTS Thin Film and Bifacial Solar Cell. *ACS Applied Materials & Interfaces* **2014**, *6* (23), 21118–21130. https://doi.org/10.1021/am505980n.
(13) Lopez-Marino, S.; Espíndola-Rodríguez, M.; Sánchez, Y.; Alcobé, X.; Oliva, F.; Xie, H.; Neuschitzer, M.; Giraldo, S.; Placidi, M.; Caballero, R.; Izquierdo-Roca, V.; Pérez-Rodríguez, A.; Saucedo, E. The Importance of Back Contact Modification in $Cu_2ZnSnSe_4$ Solar Cells: The Role of a Thin MoO_2 Layer. *Nano Energy* **2016**, *26*, 708–721. https://doi.org/10.1016/j.nanoen.2016.06.034.
(14) Wada, T.; Kohara, N.; Nishiwaki, S.; Negami, T. Characterization of the Cu(In,Ga)Se_2/Mo Interface in CIGS Solar Cells. *Thin Solid Films* **2001**, *387* (1), 118–122.
(15) Kohara, N.; Nishiwaki, S.; Hashimoto, Y.; Negami, T.; Wada, T. Electrical Properties of the Cu(In,Ga)Se_2/ $MoSe_2$/Mo Structure. *Solar Energy Materials* **2001**, 7.
(16) Hsiao, K.-J.; Liu, J.-D.; Hsieh, H.-H.; Jiang, T.-S. Electrical Impact of $MoSe_2$ on CIGS Thin-Film Solar Cells. *Physical Chemistry Chemical Physics* **2013**, *15* (41), 18174. https://doi.org/10.1039/c3cp53310g.
(17) Schnabel, T.; Ahlswede, E. On the Interface between Kesterite Absorber and Mo Back Contact and Its Impact on Solution-Processed Thin-Film Solar Cells. *Solar Energy Materials and Solar Cells* **2017**, *159*, 290–295. https://doi.org/10.1016/j.solmat.2016.09.029.

(18) Espindola-Rodriguez, M.; Sanchez, Y.; Lopez-Marino, S.; Xie, H.; Izquierdo-Roca, V.; Sylla, D.; Neuschitzer, M.; Vigil-Galan, O.; Saucedo, E.; Placidi, M. Efficient Bifacial $Cu_2ZnSnSe_4$ Solar Cells. In *2015 IEEE 42nd Photovoltaic Specialist Conference (PVSC)*; IEEE: New Orleans, LA, 2015; pp 1–3. https://doi.org/10.1109/PVSC.2015.7355903.

(19) Meyer, J.; Hamwi, S.; Kröger, M.; Kowalsky, W.; Riedl, T.; Kahn, A. Transition Metal Oxides for Organic Electronics: Energetics, Device Physics and Applications. *Advanced Materials* **2012**, *24* (40), 5408–5427. https://doi.org/10.1002/adma.201201630.

(20) Greiner, M. T.; Helander, M. G.; Tang, W.-M.; Wang, Z.-B.; Qiu, J.; Lu, Z.-H. Universal Energy-Level Alignment of Molecules on Metal Oxides. *Nature Materials* **2012**, *11* (1), 76–81. https://doi.org/10.1038/nmat3159.

(21) Paudel, N. R.; Xiao, C.; Yan, Y. CdS/CdTe Thin-Film Solar Cells with Cu-Free Transition Metal Oxide/Au Back Contacts: CdTe Cells with Cu-Free TMO/Au Back Contacts. *Progress in Photovoltaics: Research and Applications* **2015**, *23* (4), 437–442. https://doi.org/10.1002/pip.2446.

(22) Simchi, H.; McCandless, B. E.; Meng, T.; Shafarman, W. N. Structure and Interface Chemistry of MoO_3 Back Contacts in $Cu(In,Ga)Se_2$ Thin Film Solar Cells. *Journal of Applied Physics* **2014**, *115* (3), 033514. https://doi.org/10.1063/1.4862404.

(23) Antunez, P. D.; Bishop, D. M.; Luo, Y.; Haight, R. Efficient Kesterite Solar Cells with High Open-Circuit Voltage for Applications in Powering Distributed Devices. *Nature Energy* **2017**, *2* (11), 884–890. https://doi.org/10.1038/s41560-017-0028-5.

(24) Ranjbar, S.; Brammertz, G.; Vergman, B.; Hadipour, A.; Cong, S.; Suganuma, K.; Schnabel, T.; Meuris, M.; Da Cunha, A. F.; Poortmans, J. Improvement of Kesterite Solar Cell Performance by Solution Synthesized MoO_3 Interfacial Layer. *Phys. Status Solidi A* **2016**, 6.

(25) Liu, L.; Lau, T.-K.; Zhi, Z.; Huang, L.; Wang, S.; Xiao, X. Modification of Mo Back Contact with MoO_{3-x} Layer and Its Effect to Enhance the Performance of Cu_2ZnSnS_4 Solar Cells. *Solar RRL* **2018**, *2* (12), 1800243. https://doi.org/10.1002/solr.201800243.

(26) Gerling, L.; Mahato, S.; Voz, C.; Alcubilla, R.; Puigdollers, J. Characterization of Transition Metal Oxide/Silicon Heterojunctions for Solar Cell Applications. *Applied Sciences* **2015**, *5* (4), 695–705. https://doi.org/10.3390/app5040695.

(27) Gerling, L. G.; Mahato, S.; Morales-Vilches, A.; Masmitja, G.; Ortega, P.; Voz, C.; Alcubilla, R.; Puigdollers, J. Transition Metal Oxides as Hole-Selective Contacts in Silicon Heterojunctions Solar Cells. *Solar Energy Materials and Solar Cells* **2016**, *145*, 109–115. https://doi.org/10.1016/j.solmat.2015.08.028.

(28) Gerling, L. G.; Voz, C.; Alcubilla, R.; Puigdollers, J. Origin of Passivation in Hole-Selective Transition Metal Oxides for Crystalline Silicon Heterojunction Solar Cells. *Journal of Materials Research* **2017**, *32* (02), 260–268. https://doi.org/10.1557/jmr.2016.453.

(29) Almora, O.; Gerling, L. G.; Voz, C.; Alcubilla, R.; Puigdollers, J.; Garcia-Belmonte, G. Superior Performance of V_2O_5 as Hole Selective Contact over Other Transition Metal Oxides in Silicon Heterojunction Solar Cells. *Solar Energy Materials and Solar Cells* **2017**, *168*, 221–226. https://doi.org/10.1016/j.solmat.2017.04.042.

(30) Bullock, J.; Cuevas, A.; Allen, T.; Battaglia, C. Molybdenum Oxide MoO_x: A Versatile Hole Contact for Silicon Solar Cells. *Applied Physics Letters* **2014**, *105* (23), 232109. https://doi.org/10.1063/1.4903467.

(31) Greiner, M. T.; Chai, L.; Helander, M. G.; Tang, W.-M.; Lu, Z.-H. Transition Metal Oxide Work Functions: The Influence of Cation Oxidation State and Oxygen Vacancies. *Adv. Funct. Mater.* **2012**, *22* (21), 4557–4568. https://doi.org/10.1002/adfm.201200615.

(32) Xie, H.; Sánchez, Y.; López-Marino, S.; Espíndola-Rodríguez, M.; Neuschitzer, M.; Sylla, D.; Fairbrother, A.; Izquierdo-Roca, V.; Pérez-Rodríguez, A.; Saucedo, E. Impact of Sn(S,Se) Secondary Phases in $Cu_2ZnSn(S,Se)_4$ Solar Cells: A Chemical Route for Their Selective Removal and Absorber

Surface Passivation. *ACS Applied Materials & Interfaces* **2014**, *6* (15), 12744–12751. https://doi.org/10.1021/am502609c.

(33) Giraldo, S.; Neuschitzer, M.; Thersleff, T.; López-Marino, S.; Sánchez, Y.; Xie, H.; Colina, M.; Placidi, M.; Pistor, P.; Izquierdo-Roca, V.; Leifer, K.; Pérez-Rodríguez, A.; Saucedo, E. Large Efficiency Improvement in $Cu_2ZnSnSe_4$ Solar Cells by Introducing a Superficial Ge Nanolayer. *Advanced Energy Materials* **2015**. https://doi.org/10.1002/aenm.201501070.

(34) Lunt, R. R. Theoretical Limits for Visibly Transparent Photovoltaics. *Applied Physics Letters* **2012**, *101* (4), 043902. https://doi.org/10.1063/1.4738896.

(35) Oliva, F.; Kretzschmar, S.; Colombara, D.; Tombolato, S.; Ruiz, C. M.; Redinger, A.; Saucedo, E.; Broussillou, C.; de Monsabert, T. G.; Unold, T.; Dale, P. J.; Izquierdo-Roca, V.; Pérez-Rodríguez, A. Optical Methodology for Process Monitoring of Chalcopyrite Photovoltaic Technologies: Application to Low Cost $Cu(In,Ga)(S,Se)_2$ Electrodeposition Based Processes. *Solar Energy Materials and Solar Cells* **2016**, *158*, 168–183. https://doi.org/10.1016/j.solmat.2015.12.036.

(36) Anuar, K.; Zainal, Z.; Saravanan, N.; Kartini, A. R. Cathodic Electrodeposition and Characterization of Ni_3Se_2 Thin Films. *AJSTD* **2017**, *21* (1), 19. https://doi.org/10.29037/ajstd.88.

(37) Wang B.; Liu F.-Y.; Li J.; Lai Y.-Q.; Zhang Z.-A.; Liu Y.-X. Preparation and Characterization of Co-Se Thin Films by Electrodeposition. *Journal of Inorganic Materials* **2011**, *26* (4), 403–410. https://doi.org/10.3724/SP.J.1077.2011.00403.

(38) Gusakova, J.; Wang, X.; Shiau, L. L.; Krivosheeva, A.; Shaposhnikov, V.; Borisenko, V.; Gusakov, V.; Tay, B. K. Electronic Properties of Bulk and Monolayer TMDs: Theoretical Study Within DFT Framework (GVJ-2e Method). *physica status solidi (a)* **2017**, *214* (12), 1700218. https://doi.org/10.1002/pssa.201700218.

(39) Becerril-Romero, I.; Giraldo, S.; López-Marino, S.; Placidi, M.; Sánchez, Y.; Sylla, D.; Pérez-Rodríguez, A.; Saucedo, E.; Pistor, P. Vitreous Enamel as Sodium Source for Efficient Kesterite Solar Cells on Commercial Ceramic Tiles. *Solar Energy Materials and Solar Cells* **2016**, *154*, 11–17. https://doi.org/10.1016/j.solmat.2016.04.035.

(40) Becerril-Romero, I.; Acebo, L.; Oliva, F.; Izquierdo-Roca, V.; López-Marino, S.; Espíndola-Rodríguez, M.; Neuschitzer, M.; Sánchez, Y.; Placidi, M.; Pérez-Rodríguez, A.; Saucedo, E.; Pistor, P. CZTSe Solar Cells Developed on Polymer Substrates: Effects of Low-Temperature Processing. *Progress in Photovoltaics: Research and Applications* **2017**. https://doi.org/10.1002/pip.2945.

(41) Dimitrievska, M.; Gurieva, G.; Xie, H.; Carrete, A.; Cabot, A.; Saucedo, E.; Pérez-Rodríguez, A.; Schorr, S.; Izquierdo-Roca, V. Raman Scattering Quantitative Analysis of the Anion Chemical Composition in Kesterite $Cu_2ZnSn(S_xSe_{1-x})_4$ Solid Solutions. *Journal of Alloys and Compounds* **2015**, *628*, 464–470. https://doi.org/10.1016/j.jallcom.2014.12.175.

(42) Andrade-Arvizu, J.; Izquierdo-Roca, V.; Becerril-Romero, I.; Vidal-Fuentes, P.; Fonoll-Rubio, R.; Sánchez, Y.; Placidi, M.; Calvo-Barrio, L.; Vigil-Galán, O.; Saucedo, E. Is It Possible To Develop Complex S–Se Graded Band Gap Profiles in Kesterite-Based Solar Cells? *ACS Appl. Mater. Interfaces* **2019**, *11* (36), 32945–32956. https://doi.org/10.1021/acsami.9b09813.

(43) Caballero, R.; Nichterwitz, M.; Steigert, A.; Eicke, A.; Lauermann, I.; Schock, H. W.; Kaufmann, C. A. Impact of Na on $MoSe_2$ Formation at the CIGSe/Mo Interface in Thin-Film Solar Cells on Polyimide Foil at Low Process Temperatures. *Acta Materialia* **2014**, *63*, 54–62. https://doi.org/10.1016/j.actamat.2013.09.051.

(44) Rockett, A.; Granath, K.; Asher, S.; Jassim, M. M. A.; Hasoon, F.; Matson, R.; Basol, B.; Kapur, V.; Britt, J. S.; Gillespie, T.; Marshall, C. Na Incorporation in Mo and $CuInSe_2$ from Production Processes. *Solar Energy Materials and Solar Cells* **1999**, *59* (3), 255–264. https://doi.org/10.1016/S0927-0248(99)00026-4.

(45) Brus, L. E. Electron–Electron and Electron-hole Interactions in Small Semiconductor Crystallites: The Size Dependence of the Lowest Excited Electronic State. *The Journal of Chemical Physics* **1984**, *80* (9), 4403–4409. https://doi.org/10.1063/1.447218.

(46) Fairbrother, A.; Izquierdo-Roca, V.; Fontané, X.; Ibáñez, M.; Cabot, A.; Saucedo, E.; Pérez-Rodríguez, A. ZnS Grain Size Effects on Near-Resonant Raman Scattering: Optical Non-Destructive Grain Size Estimation. *CrystEngComm* **2014**, *16* (20), 4120. https://doi.org/10.1039/c3ce42578a.

(47) Baskoutas, S.; Terzis, A. F. Size-Dependent Band Gap of Colloidal Quantum Dots. *Journal of Applied Physics* **2006**, *99* (1), 013708. https://doi.org/10.1063/1.2158502.

(48) Jain, P.; Arun, P. Influence of Grain Size on the Band-Gap of Annealed SnS Thin Films. *Thin Solid Films* **2013**, *548*, 241–246. https://doi.org/10.1016/j.tsf.2013.09.089.

(49) Dimitrievska, M.; Fairbrother, A.; Pérez-Rodríguez, A.; Saucedo, E.; Izquierdo-Roca, V. Raman Scattering Crystalline Assessment of Polycrystalline Cu_2ZnSnS_4 Thin Films for Sustainable Photovoltaic Technologies: Phonon Confinement Model. *Acta Materialia* **2014**, *70*, 272–280. https://doi.org/10.1016/j.actamat.2014.02.035.

(50) Lim, Y.-F.; Choi, J. J.; Hanrath, T. Facile Synthesis of Colloidal CuO Nanocrystals for Light-Harvesting Applications. *Journal of Nanomaterials* **2012**, *2012*, 1–6. https://doi.org/10.1155/2012/393160.

(51) Arun, K. J.; Batra, A. K.; Krishna, A.; Bhat, K.; Aggarwal, M. D.; Francis, P. J. J. Surfactant Free Hydrothermal Synthesis of Copper Oxide Nanoparticles. *Am. J. Mater. Sci.* **2015**, *5(3A)*, 36–38. https://doi.org/10.5923/s.materials.201502.06.

(52) He, X.; Song, X.; Qiao, W.; Li, Z.; Zhang, X.; Yan, S.; Zhong, W.; Du, Y. Phase- and Size-Dependent Optical and Magnetic Properties of CoO Nanoparticles. *J. Phys. Chem. C* **2015**, *119* (17), 9550–9559. https://doi.org/10.1021/jp5127909.

(53) Temgoua, S.; Bodeux, R.; Naghavi, N.; Delbos, S. Effects of $SnSe_2$ Secondary Phases on the Efficiency of $Cu_2ZnSn(S_x,Se_{1-x})_4$ Based Solar Cells. *Thin Solid Films* **2015**, *582*, 215–219. https://doi.org/10.1016/j.tsf.2014.10.058.

(54) Guo, L.; Zhu, Y.; Gunawan, O.; Gokmen, T.; Deline, V. R.; Ahmed, S.; Romankiw, L. T.; Deligianni, H. Electrodeposited $Cu_2ZnSnSe_4$ Thin Film Solar Cell with 7% Power Conversion Efficiency: Power Conversion Efficiency of $Cu_2ZnSnSe_4$. *Prog. Photovolt: Res. Appl.* **2014**, *22* (1), 58–68. https://doi.org/10.1002/pip.2332.

(55) Sutter-Fella, C. M.; Stückelberger, J. A.; Hagendorfer, H.; La Mattina, F.; Kranz, L.; Nishiwaki, S.; Uhl, A. R.; Romanyuk, Y. E.; Tiwari, A. N. Sodium Assisted Sintering of Chalcogenides and Its Application to Solution Processed $Cu_2ZnSn(S,Se)_4$ Thin Film Solar Cells. *Chemistry of Materials* **2014**, *26* (3), 1420–1425. https://doi.org/10.1021/cm403504u.

(56) Gershon, T.; Shin, B.; Bojarczuk, N.; Hopstaken, M.; Mitzi, D. B.; Guha, S. The Role of Sodium as a Surfactant and Suppressor of Non-Radiative Recombination at Internal Surfaces in Cu_2ZnSnS_4. *Advanced Energy Materials* **2015**, *5* (2), n/a-n/a. https://doi.org/10.1002/aenm.201400849.

(57) Yang, K.-J.; Sim, J.-H.; Jeon, B.; Son, D.-H.; Kim, D.-H.; Sung, S.-J.; Hwang, D.-K.; Song, S.; Khadka, D. B.; Kim, J.; Kang, J.-K. Effects of Na and MoS_2 on Cu_2ZnSnS_4 Thin-Film Solar Cell. *Progress in Photovoltaics: Research and Applications* **2015**, *23* (7), 862–873. https://doi.org/10.1002/pip.2500.

(58) Li, J. B.; Chawla, V.; Clemens, B. M. Investigating the Role of Grain Boundaries in CZTS and CZTSSe Thin Film Solar Cells with Scanning Probe Microscopy. *Advanced Materials* **2012**, *24* (6), 720–723. https://doi.org/10.1002/adma.201103470.

(59) Kröger, M.; Hamwi, S.; Meyer, J.; Riedl, T.; Kowalsky, W.; Kahn, A. P-Type Doping of Organic Wide Band Gap Materials by Transition Metal Oxides: A Case-Study on Molybdenum Trioxide. *Organic Electronics* **2009**, *10* (5), 932–938. https://doi.org/10.1016/j.orgel.2009.05.007.

(60) Laubach, S.; Schmidt, P. C.; Thißen, A.; Fernandez-Madrigal, F. J.; Wu, Q.-H.; Jaegermann, W.; Klemm, M.; Horn, S. Theoretical and Experimental Determination of the Electronic Structure of

V_2O_5 , Reduced V_2O_{5-x} and Sodium Intercalated NaV_2O_5. *Phys. Chem. Chem. Phys.* **2007**, *9* (20), 2564–2576. https://doi.org/10.1039/B612489E.

(61) Uozumi, T.; Okada, K.; Kotani, A. Electronic Structures of Ti and V Oxides: Calculation of Valence Photoemission and Bremsstrahlung Isochromat Spectra. *Journal of the Physical Society of Japan* **1993**, *62* (8), 2595–2599. https://doi.org/10.1143/JPSJ.62.2595.

(62) Zimmermann, R.; Steiner, P.; Claessen, R.; Reinert, F.; Hüfner, S.; Blaha, P.; Dufek, P. Electronic Structure of 3d-Transition-Metal Oxides: On-Site Coulomb Repulsion versus Covalency. *Journal of Physics: Condensed Matter* **1999**, *11* (7), 1657–1682. https://doi.org/10.1088/0953-8984/11/7/002.

(63) van Elp, J.; Wieland, J. L.; Eskes, H.; Kuiper, P.; Sawatzky, G. A.; de Groot, F. M. F.; Turner, T. S. Electronic Structure of CoO, Li-Doped CoO, and $LiCoO_2$. *Physical Review B* **1991**, *44* (12), 6090–6103. https://doi.org/10.1103/PhysRevB.44.6090.

(64) Saha, U.; Alam, Md. K. Proposition and Computational Analysis of a Kesterite/Kesterite Tandem Solar Cell with Enhanced Efficiency. *RSC Adv.* **2017**, *7* (8), 4806–4814. https://doi.org/10.1039/C6RA25704F.

(65) Helander, M. G.; Greiner, M. T.; Wang, Z. B.; Tang, W. M.; Lu, Z. H. Work Function of Fluorine Doped Tin Oxide. *Journal of Vacuum Science & Technology A: Vacuum, Surfaces, and Films* **2011**, *29* (1), 011019. https://doi.org/10.1116/1.3525641.

Table 1. Main optoelectronic properties of the TMOs employed in this work.

	Semiconductor type	Ionization Energy (eV)	Bandgap (eV)	Work function (eV)	Reference
MoO_3	n	9.4	3.0	6.9	[59]
V_2O_5	n	9.3	2.8	6.9	[60]
TiO_2	n	8.0	3.4	5.2	[61]
NiO	p	6.7	3.2	6.3	[62]
Co_3O_4	p	6.4	1.6	6.1	[63]
CuO	p	5.7	1.4	5.6	[62]

Table 2. Reactive annealing parameters for kesterite absorber synthesis.

Absorber	Box volume (cm^3)	Se (mg)	S (mg)	Sn (mg)	Step	p (mbar)	Ar flow	Ramp (°C/min)	T (°C)	t (min)
CZTSe	69	100	-	5	1	1.5	Yes	20	400	30
					2	1000	No	20	550	15
CZTSSe	23.5	2	48	5	1	1.5	Yes	20	250	20
					2	1000	No	20	550	40
CZTS	69	-	50	5	1	1.5	Yes	20	200	15
					2	1000	No	20	550	40

Table 3. Optoelectronic parameters of the record devices obtained with each substrate configuration. The rows in bold correspond to the best configuration obtained with each TMO.

Substrate configuration	TMO thickness (nm)	J_{sc} (mA/cm^2)	V_{oc} (mV)	FF (%)	η (%)	R_{sh} ($\Omega \cdot cm^2$)	R_s ($\Omega \cdot cm^2$)
FTO	-	31.5	263	46.3	3.8	60	0.8
FTO/Mo:Na	-	32.7	315	48.9	5.0	230	1.4
FTO/TiO_2/Mo:Na	5	35.0	346	49.1	5.9	270	1.4
	10	**34.4**	**355**	**50.9**	**6.2**	**520**	**1.5**
	20	33.1	355	49.5	5.8	160	1.1
FTO/V_2O_5/Mo:Na	5	32.8	316	45.2	4.7	170	1.7
	10	**33.8**	**328**	**48.7**	**5.4**	**240**	**1.4**
	20	30.2	315	49.5	4.7	270	1.0

Table 4. Optoelectronic parameters of the record devices obtained with each substrate configuration and kesterite absorber in Series B and C. The rows in bold correspond to the best configuration obtained for each absorber.

Absorber	Substrate configuration	J_{sc} (mA/cm^2)	V_{oc} (mV)	FF (%)	η (%)	R_{sh} (Ω·cm^2)	R_s (Ω·cm^2)
CZTSe	FTO	31.5	263	46.3	3.8	60	0.8
	FTO/Mo:Na	32.7	315	48.9	5.0	230	1.4
	FTO/TiO_2/Mo:Na	**34.4**	**355**	**50.9**	**6.2**	**520**	**1.5**
	FTO/V_2O_5/Mo:Na	33.8	328	48.7	5.4	240	1.4
CZTS	FTO	17.2	579	37.4	3.7	60	4.5
	FTO/Mo:Na	**14.6**	**755**	**55.2**	**6.1**	**320**	**1.7**
	FTO/TiO_2/Mo:Na	11.3	542	42.3	2.6	170	8.7
	FTO/V_2O_5/Mo:Na	15.2	618	41.5	3.9	110	1.8
CZTSSe	FTO	17.1	546	35.2	3.3	100	13.8
	FTO/Mo:Na	18.1	617	46.4	5.2	180	2.9
	FTO/TiO_2/Mo:Na	18.9	589	58.0	6.4	320	3.3
	FTO/V_2O_5/Mo:Na	**21.7**	**620**	**58.8**	**7.9**	**270**	**1.8**

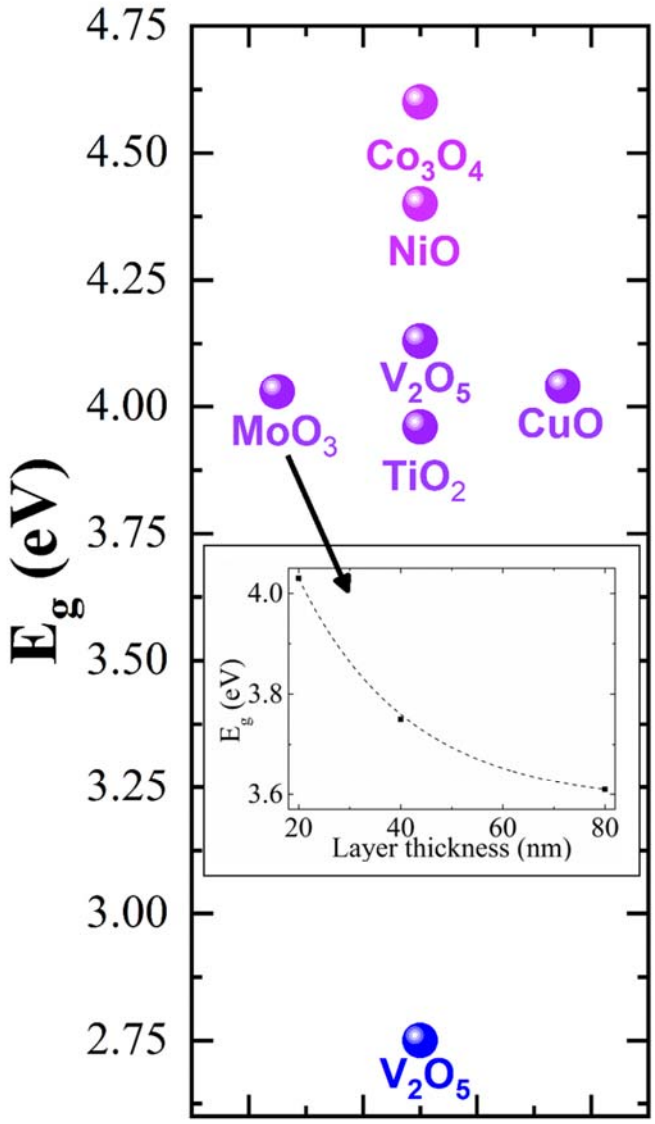

Figure 1. Bandgap of the different TMOs deposited (20 nm layers) on quartz and extracted from their transmittance spectra (see Figure S2). The two values of V_2O_5 correspond to two inflection points found in its transmittance spectra. Inset: bandgap of MoO_3 layers with different thicknesses.

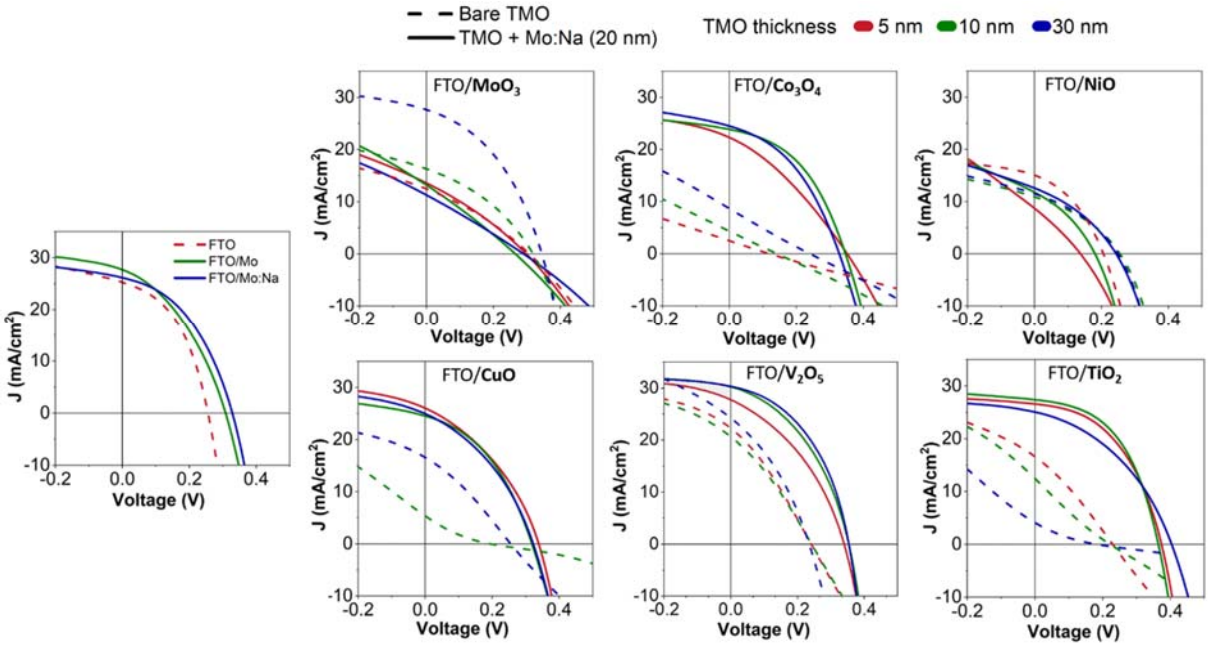

Figure 2. J-V curves of the CZTSe devices fabricated on the different substrate configurations containing different TMO thicknesses. Dashed lines represent devices to which no Mo-based layers were added (labelled as "Bare TMOs"). Solid lines represent the devices that contain a combination of TMO and a 20 nm Mo:Na layer.

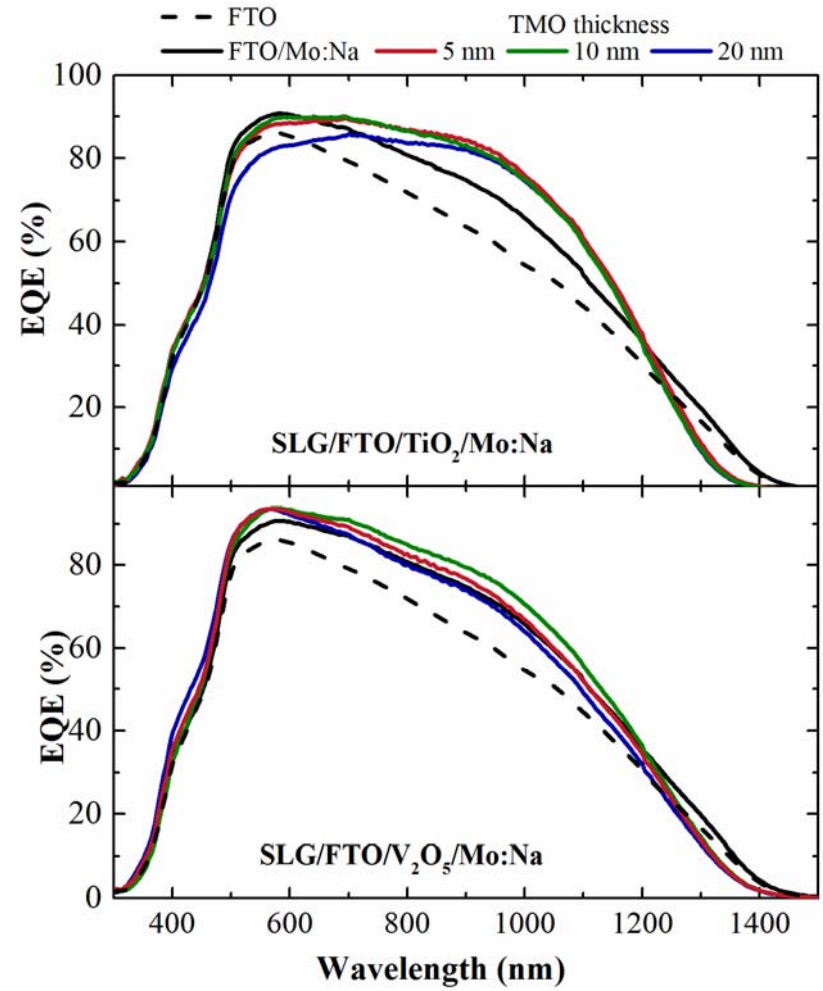

Figure 3. EQE of the record devices obtained in Series B with each substrate configuration.

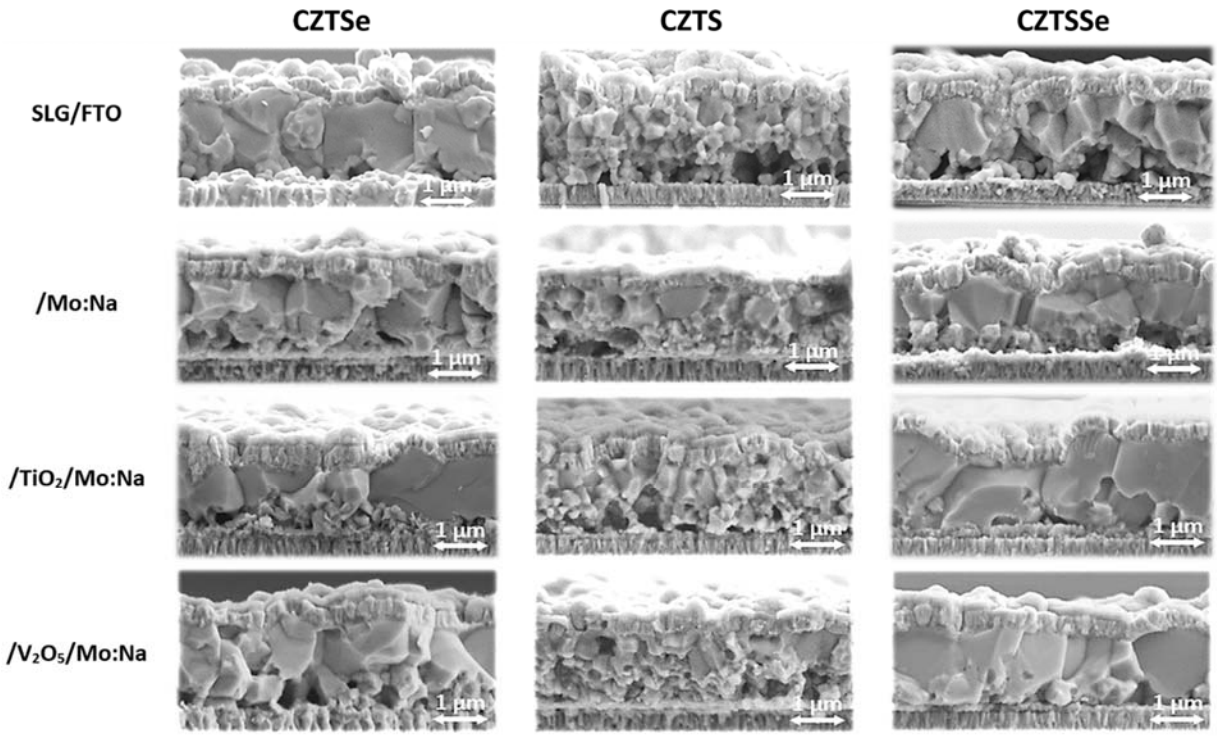

Figure 4. Cross-sectional FESEM micrographs of the best performing CZTSe (Series B), CZTS (Series C) and CZTSSe (Series C) devices fabricated on the different substrate configurations.

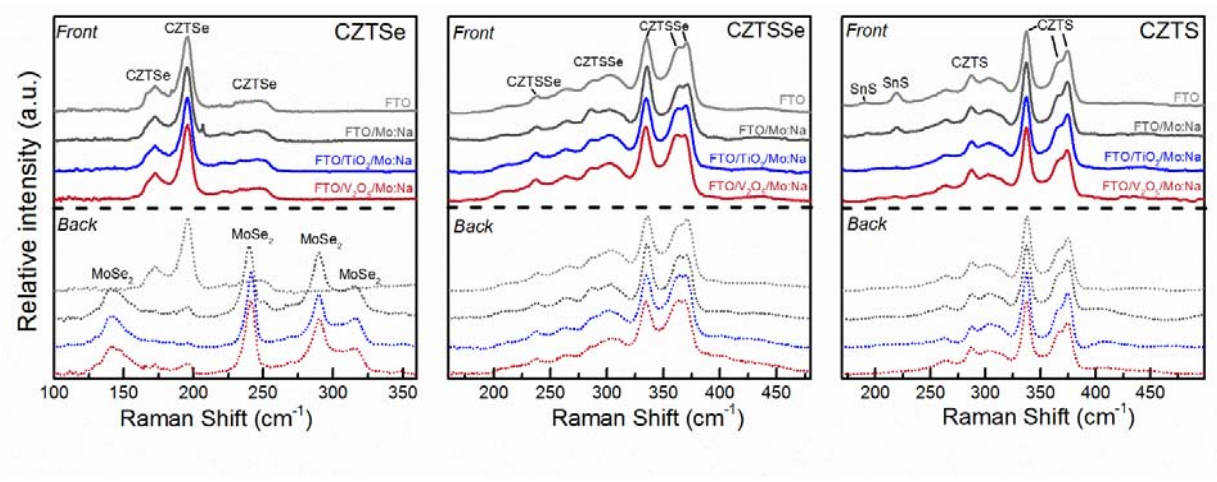

Figure 5. Raman spectra of the of the best performing CZTSe (Series B), CZTS (Series C) and CZTSSe (Series C) devices fabricated on the different substrate configurations. The measurements

were carried out at the front surface (continuous lines) and the back surface (dotted lines) employing λ_{ex} = 785 nm.

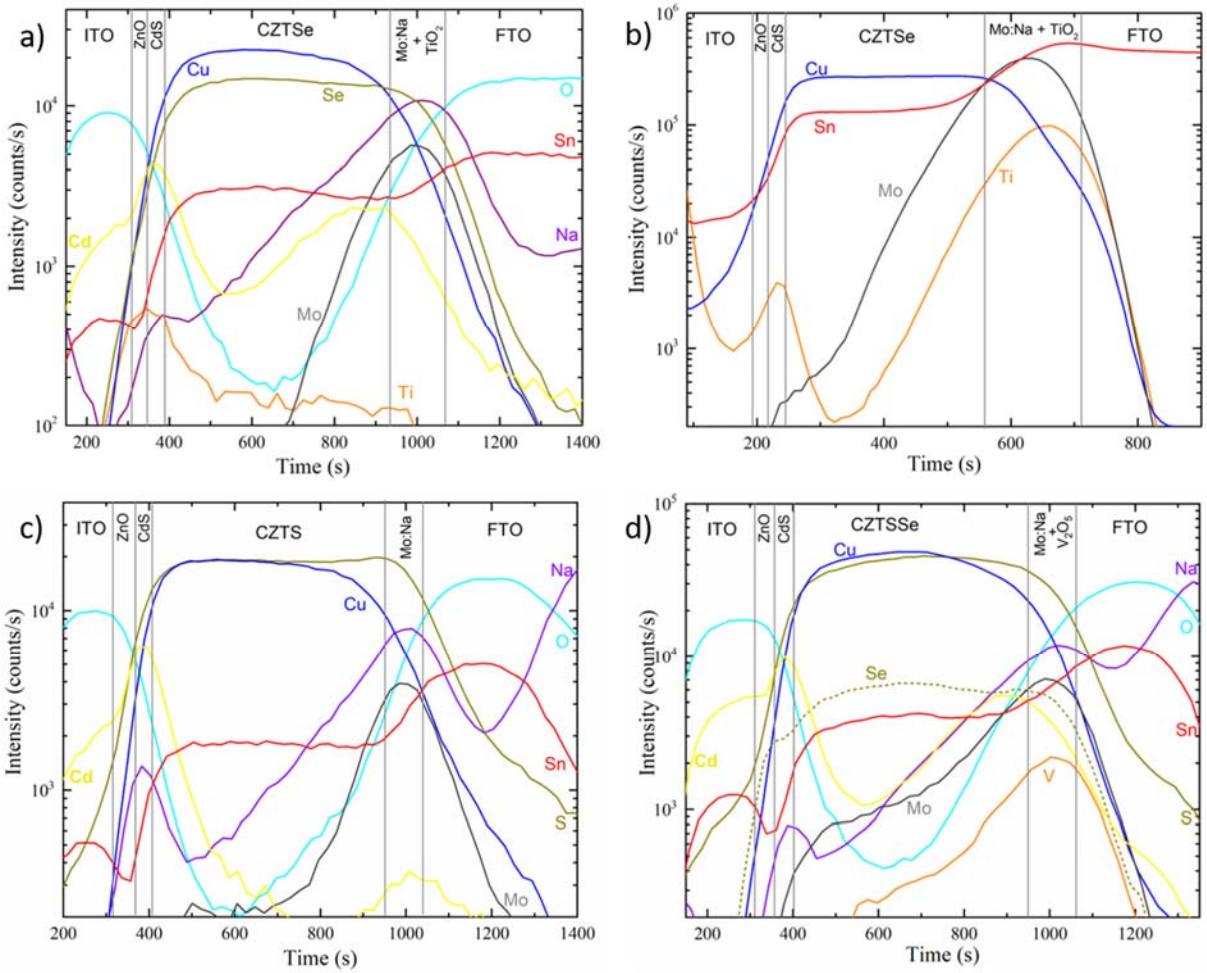

Figure 6. SIMS spectra of the best CZTSe (a), CZTS (c) and CZTSSe (d) performing devices fabricated on SLG/FTO/TiO_2/Mo:Na, SLG/FTO/Mo:Na and SLG/FTO/V_2O_5/Mo:Na, respectively, obtained using a Cs^+ primary beam. b) CZTSe spectrum obtained using a O_2^+ primary beam. The boundaries between the different layers shown in the spectra are only intended as a visual guide for the reader.

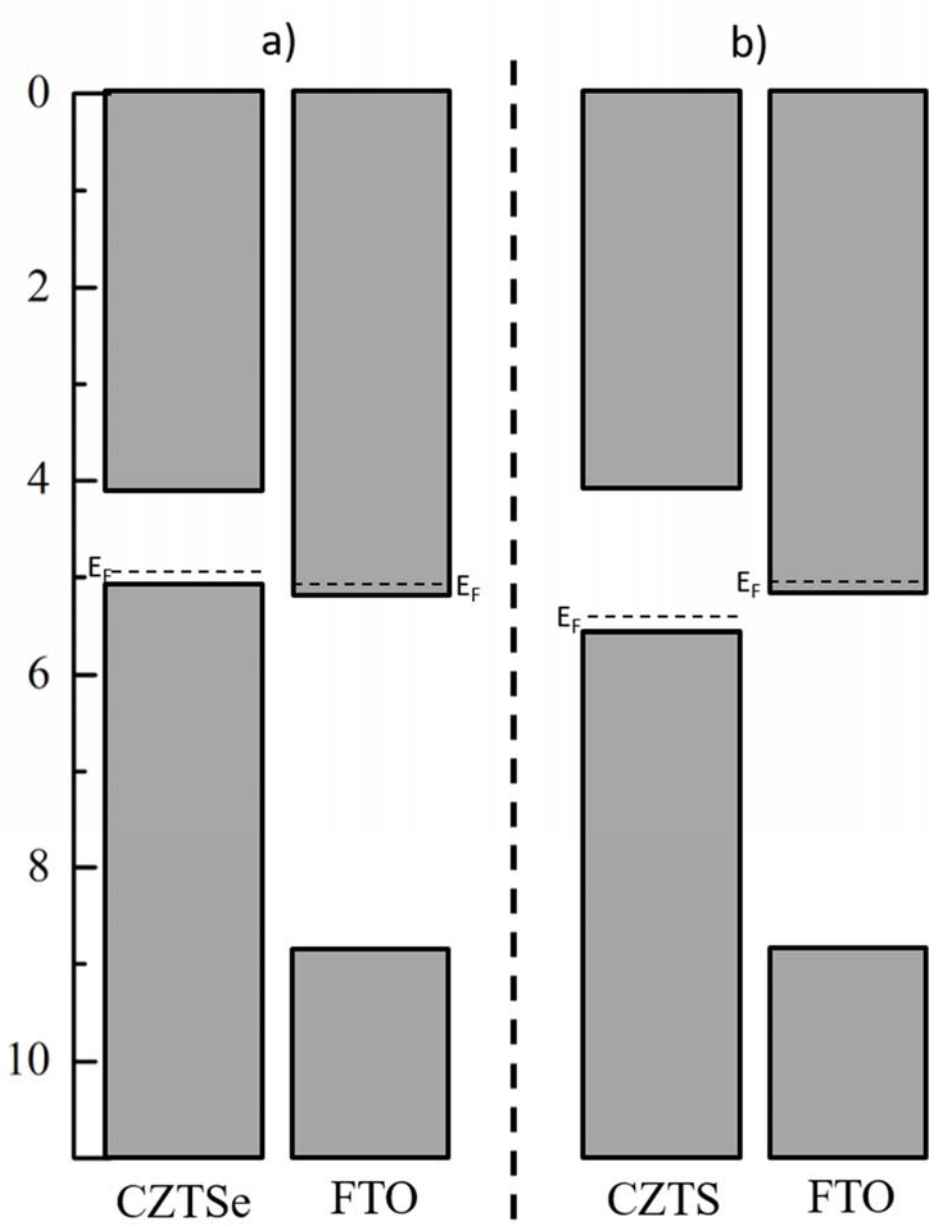

Figure 7. Band diagrams of CZTSe, CZTS and FTO. Data sources: [64,65].

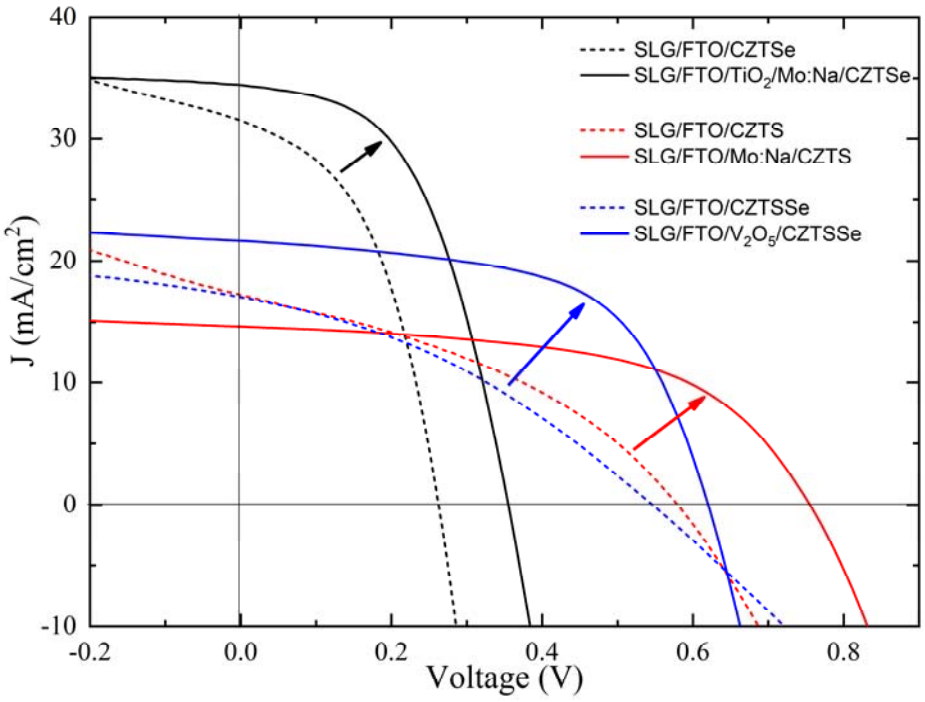

Figure 8. Reference (dashed) and record (solid) J-V curves obtained for CZTSe, CZTS and CZTSSe devices fabricated on SLG/FTO.